ORIGINAL ARTICLE

Hydrothermal Synthesis of Fe-Doped Nickel Cobalt Phosphate Nanofibers for High-Stability Electrochemical Overall Water Splitting

Suraj A. Khalate[1] · Thach N. Tu[1,2] · Jinsoo Kim[1]

Abstract

In this study, we synthesized new iron-doped nickel cobalt phosphate nanofibers, deposited them on nickel foam (NF), and deployed them as active catalysts for oxygen evolution reactions (OERs), hydrogen evolution reactions (HERs), and overall water splitting. Our catalyst, the Fe-doped nickel cobalt phosphate nanofiber at 1.05 Fe atom% (Fe-1.05), exhibited a Brunauer–Emmett–Teller surface area (BET SA) of 57.0 $m^2\,g^{-1}$ and a Barrett−Joyner−Halenda (BJH) mesopore of 3.7 nm. Because of its large surface area and mesopore architecture, which facilitate ionic diffusion, NF-deposited Fe-1.05 (Fe-1.05@NF) exhibited exceptional OER ($\eta = 234$ mV @ 10 mA cm^{-2}) and HER ($\eta = 104$ mV @ 10 mA cm^{-2}) performance. Overall water splitting analysis showed the lowest potentials of 1.59, 1.76, and 1.86 V at 10, 50, and 100 mA cm^{-2}, respectively. These results show the superior OER and HER performance of Fe-1.05@NF over that of the best-performing nickel cobalt phosphates and their Fe-dopped analogs in the literature. A stability test for overall water splitting for 100 h in a 1-M KOH electrolyte at a current density of 100 mA cm^{-2} demonstrated remarkable durability. The enhanced electrochemical activity of Fe-1.05@NF can be attributed to the synergistic effect between the metal atoms and phosphate ligands, which facilitates favorable conditions for the adsorption and oxidation of electrolyte ions, enhanced electrical conductivity, and active site availability due to Fe (dopant) metal atoms, providing a nanostructured (nanofiber) morphology with high porosity.

Keywords Oxygen evolution reactions · Hydrogen evolution reactions · Overall water splitting · Metal phosphate materials · Nanofibers

Introduction

Hydrogen, characterized by its high calorific value upon combustion and environmental friendliness, is emerging as a highly promising contender in the field of renewable energy sources [1, 2]. Water electrolysis driven by renewable electrical energy for hydrogen production is a sustainable and emission-free approach that aligns with the objectives of carbon neutrality [3]. In principle, water electrolysis involves two major processes: (i) the hydrogen evolution reaction (HER) at the cathode and (ii) the oxygen evolution reaction (OER) at the anode. However, the sluggishness of OER leads to elevated energy consumption levels [4]. Therefore, the development of a stable and robust OER catalyst is critical for improving the overall efficiency of hydrogen generation. Conventionally, state-of-the-art materials such as IrO_2 and RuO_2 have been extensively used for OER because of their high efficiency [5, 6]. However, their rarity and limited stability, particularly at higher anodic potentials, have posed considerable obstacles to the advancement of water electrolysis technology [7]. To overcome these challenges, researchers have redirected their efforts toward exploring first-row transition metal compounds that are more readily available [8–11]. Metal oxides [12], hydroxides [13], metal sulfides [14], nitrides [15], and phosphides [16] and metal−nitrogen−carbon materials [17, 18] have been explored in recent decades as effective electrocatalysts for water splitting. Among these, transition metal phosphates [19] are promising catalysts for electrochemical water splitting. Transition

Suraj A. Khalate, Thach N. Tu have contributed equally.

✉ Jinsoo Kim
  jkim21@khu.ac.kr

1 Department of Chemical Engineering (Integrated Engineering), Kyung Hee University, 1732 Deogyeong-daero, Giheung-Gu, Yongin-si, Gyeonggi-do 17104, Republic of Korea

2 Nguyen Tat Thanh University, 300A Nguyen Tat Thanh Street, District 4, Ho Chi Minh City 755414, Vietnam

metal phosphates play a pivotal role in assisting the OER, for example, facilitating adsorption and stabilizing active centers, creating conducive conditions for the adsorption of electrolyte ions and their subsequent oxidation. These effects are achieved by distorting the local atomic geometry, which facilitates the oxidation of metal atoms during proton-coupled electron transfer [20].

Nickel cobalt phosphate (NiCoPi) materials have been used as electrocatalysts; however, they still suffer from large overpotential and low stability. Several scholars have reported nickel cobalt phosphate as an electrocatalyst for OER and HER. Zhang et al. [21] reported $NiCo_2(PO_4)_2$ mesoporous hollow shells synthesized using the microwave-assisted oil-in-water emulsion method for OER in KOH (1 M) with an overpotential of 347 mV at a current density of 10 mA cm^{-2}. Septiani et al. [22] reported the self-assembly of two-dimensional (2D) nanostructures into one-dimensional nanoarchitectures of nickel cobalt phosphate synthesized using the mild solvothermal method, followed by calcination. Using KOH (1 M) electrolyte, The synthesized nickel cobalt phosphate delivered a current density of 10 mA cm^{-2} at an overpotential of 310 mV. Septiani et al. also reported that Co-rich nickel cobalt hydrogen phosphate micro spindles required an overpotential of 320 mV for the OER in KOH (1 M) [23]. CoNi-layered double hydroxide-converted $(Co_{0.5}Ni_{0.5})_3(PO_4)_2$ micro flowers were employed as OER catalysts, which required an overpotential of 273 mV to reach a current density of 10 mA cm^{-2} in KOH (1 M) [24]. Employing the polyalcohol refluxing method to synthesize nickel cobalt phosphate micro rods wrapped by 2D flakes required an overpotential of 378 mV to reach a current density of 10 mA cm^{-2} in KOH

(3 M) [25]. Meng et al. synthesized an electrodeposited thin nanosheet nanoflower, such as nickel cobalt phosphate, and applied it to self-powered water splitting [26]. Using KOH (1 M) electrolyte, the prepared electrode delivered a current density of 10 mA cm^{-2} at OER overpotential of 309 mV, whereas it required an overpotential of 236 mV to reach a current density of 10 mA cm^2 for the HER. Xu et al. synthesized self-assembled Ni/Co phosphate composite spheres that delivered a current density of 10 mA cm^{-2} by applying an overpotential of 160 mV for the HER in H_2SO_4 (0.5 M) [27]. Singh et al. synthesized ultrathin and amorphous cobalt nickel phosphate (CoNiPO$_x$) nanosheet arrays, which were then deposited on vanadium (V)-doped cobalt nitride ($V_{3\%}$–Co$_4$N) crystalline core nanowires to obtain amorphous-shell@crystalline-core mesoporous 3D heterostructures (CoNiPO$_x$@V-Co$_4$N/NF) as bifunctional electrocatalysts [28]. The prepared electrocatalyst exhibited HER and OER overpotentials in KOH (1 M) of 53 and 270 mV to deliver a current of 10 mA cm^{-2}, respectively. These studies reported a large overpotential for OER/HER using nickel cobalt phosphate. Compared with other structures, nanofibers are promising candidates for electrochemical applications [29] because of their large length-to-diameter ratio, which results in enormous porosity and surface areas, high electrical conducting pathways, and large electrode–electrolyte interface areas [30].

Introducing defects is a highly effective approach for improving the electrochemical performance of electrocatalysts. Various strategies have been developed for defect activation, including doping (introducing foreign elements), creating vacancies (removing atoms or ions), and applying strain [31–33]. These strategies are designed to finely adjust the electronic structure and modulate the binding energy between active sites and intermediates involved in the OER and HER. Because of the similar atomic structures of the 8th(VIII), 9th(VIII), and 10th(VIII) subgroup elements in the periodic table, synthesizing OER catalysts from a mixture of cations such as Ni, Co, and Fe can significantly enhance the electrocatalytic activity for water splitting. Some benefits include improved electrical conductivity, favorable electronic redistribution, creation of high-valence active centers, and the introduction of lattice strain and distortion. Consequently, these benefits result in higher current densities, reduced overpotential, improved electrical conductivity, and improved adsorption of reactants on the catalyst surface [34, 35]. Furthermore, dopant atoms can exhibit synergistic effects among multiple elements and function as new active sites, further improving catalytic performance [36]. Moreover, this allows the preservation of the original morphology and surface characteristics of transition metal compounds. The doping strategy helps maintain the desired structural integrity and properties while
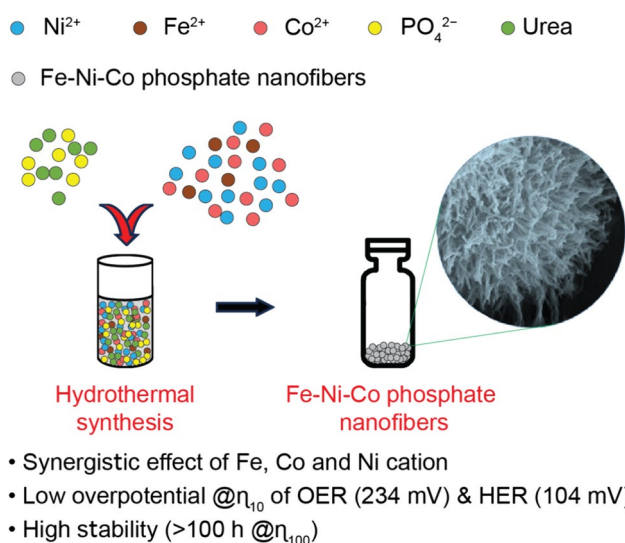

- Ni^{2+} ● Fe^{2+} ● Co^{2+} ○ PO$_4^{2-}$ ● Urea

○ Fe-Ni-Co phosphate nanofibers

Hydrothermal synthesis → Fe-Ni-Co phosphate nanofibers

- Synergistic effect of Fe, Co and Ni cation
- Low overpotential @η$_{10}$ of OER (234 mV) & HER (104 mV)
- High stability (>100 h @η$_{100}$)

Fig. 1 Schematic of synthesis of Fe-doped nickel cobalt phosphate nanofibers

improving catalytic performance in various applications, including electrocatalysis.

In this study, we report a hydrothermal procedure for synthesizing Fe-doped nickel cobalt phosphate from 0.00 to 1.46 Fe atom% (Fe-0.00 to Fe-1.46) and their deposition on NF (Fe-0.00 to Fe-1.46@NF, respectively). The resulting catalysts are characterized using nanofiber morphology, of which an exceptionally small fiber size of 20 nm is found. This unique morphology leads to the emergence of micro/meso-porosity in Fe-doped nickel cobalt phosphate nanofibers. In particular, the optimized sample (Fe-1.05) exhibited a Brunauer–Emmett–Teller surface area (BET SA) of 57.0 $m^2 g^{-1}$ and a Barrett–Joyner–Halenda (BJH) mesopore of 3.7 nm. Electrochemical catalysis investigations of Fe-1.05@NF in KOH (1 M) resulted in overpotentials of 234 mV (OER) and 104 mV (HER) at a current density of 10 mA cm^{-2}. Moreover, the Fe-1.05@NF sample exhibited potentials of 1.59, 1.76, and 1.86 V for overall water splitting at 10, 50, and 100 mA cm^{-2}, respectively. Interestingly, because of its high surface area and the presence of mesopores facilitating the diffusion of ion reagents, Fe-1.05@NF exhibited superior OER and HER performance over the best-performing nickel cobalt phosphates and their Fe-doped analogs in the literature [21–28]. In particular, Fe-1.05@NF outperformed similar NiCoFe phosphate 2D nanosheets (overpotentials of 240 and 231 mV for OER and HER, respectively) [37]. Furthermore, the durability of the water-splitting process was evaluated over 100 h, which displayed consistently outstanding performance. This study shows that the newly developed iron-doped nickel cobalt phosphate nanofiber electrodes synthesized through our innovative approach are not only cost-effective and robust but also excellent in electrochemical water electrolysis.

Experimental

Materials

Ferrous chloride ($FeCl_2$, 98%), cobalt(II) chloride hexahydrate ($CoCl_2 \cdot 6H_2O$, 98%), nickel(II) chloride ($NiCl_2$, 98%), urea ($CO(NH_2)_2$, > 98%), and potassium dihydrogen orthophosphate (KH_2PO_4, ≥ 99%) were obtained from Sigma-Aldrich.

Synthesis of *Iron*-Doped Nickel Cobalt Phosphate Nanofibers

Precursor solutions of $NiCl_2$ (5 mM), $CoCl_2 \cdot 6H_2O$ (5 mM), and KH_2PO_4 (15 mM) were separately prepared in deionized water (20 ml). An excess amount of KH_2PO_4 was used to avoid unnecessary hydroxide formation. 15 ml of the hydrolyzing agent urea (0.01 g) was added separately to the metal precursor solution, followed by continuous stirring for 15 min. The dopant $FeCl_2$ was added directly in different amounts (0.00, 0.05, 0.1, 0.15, 0.2, and 0.25 mM) for different doping concentrations and termed Fe-0.00, Fe-0.45, Fe-0.73, Fe-1.05, Fe-1.21, and Fe-1.46, respectively. The final solution (75 ml) was stirred continuously for 30 min at room temperature and then transferred to a Teflon liner (NF was optionally included in the deposition process). The autoclave was heated at 130 °C for 12 h. After finishing the reaction, the autoclave was cooled naturally to room temperature, and the samples were washed several times using deionized water and dried at 70 °C overnight for further characterization.

Deposition of *Iron*-Doped Nickel Cobalt Phosphate Nanofibers on Ni Foam

The process began with thorough cleaning of the NF substrates. A bare NF plate was then immersed in an HCl solution (5 M), which was sonicated for 15 min. This step was essential to remove any surface oxides that had formed. Subsequently, the cleaned substrates were rinsed multiple times using deionized water under sonication and were left to air dry at room temperature. These well-prepared NF substrates were subsequently used for depositing Fe-dopped nickel cobalt phosphate nanofibers. In this process, the nanofiber catalysts were prepared using a previously identified procedure, with the well-cleaned NF kept vertically in the Teflon liner following the chemical mixing and stirring steps.

Characterization methods

The as-synthesized materials were subjected to various analytical techniques for comprehensive characterization. Powder X-ray diffraction data were collected using a Rigaku diffractometer (PXRD; Miniflex 600, Rigaku Co., Japan) with Cu-Kα radiation ($\lambda = 1.5406$ Å) within a 2θ range spanning from 5° to 80°. Fourier-transform infrared spectroscopy was collected using a PerkinElmer spectrometer (FT-IR, Frontier model, PerkinElmer Co., USA) in the wavenumber range of 400–4000 cm^{-1}. N_2 adsorption–desorption isotherms and surface analysis was analyzed using a Belsorp Max instrument (Microtrac BEL Corp., Japan). Field emission scanning electron microscopy (FE-SEM; Merlin, Carl Zeiss, Germany) was used to investigate the composition and surface morphology of the materials. Field emission transmission electron microscopy (TEM) and high-resolution TEM (HR-TEM) analyses were performed using JEM-ARM200F (JEOL Ltd. Japan) with an acceleration voltage of 200 kV. X-ray photoelectron spectroscopy was performed using an X-ray Photoelectron
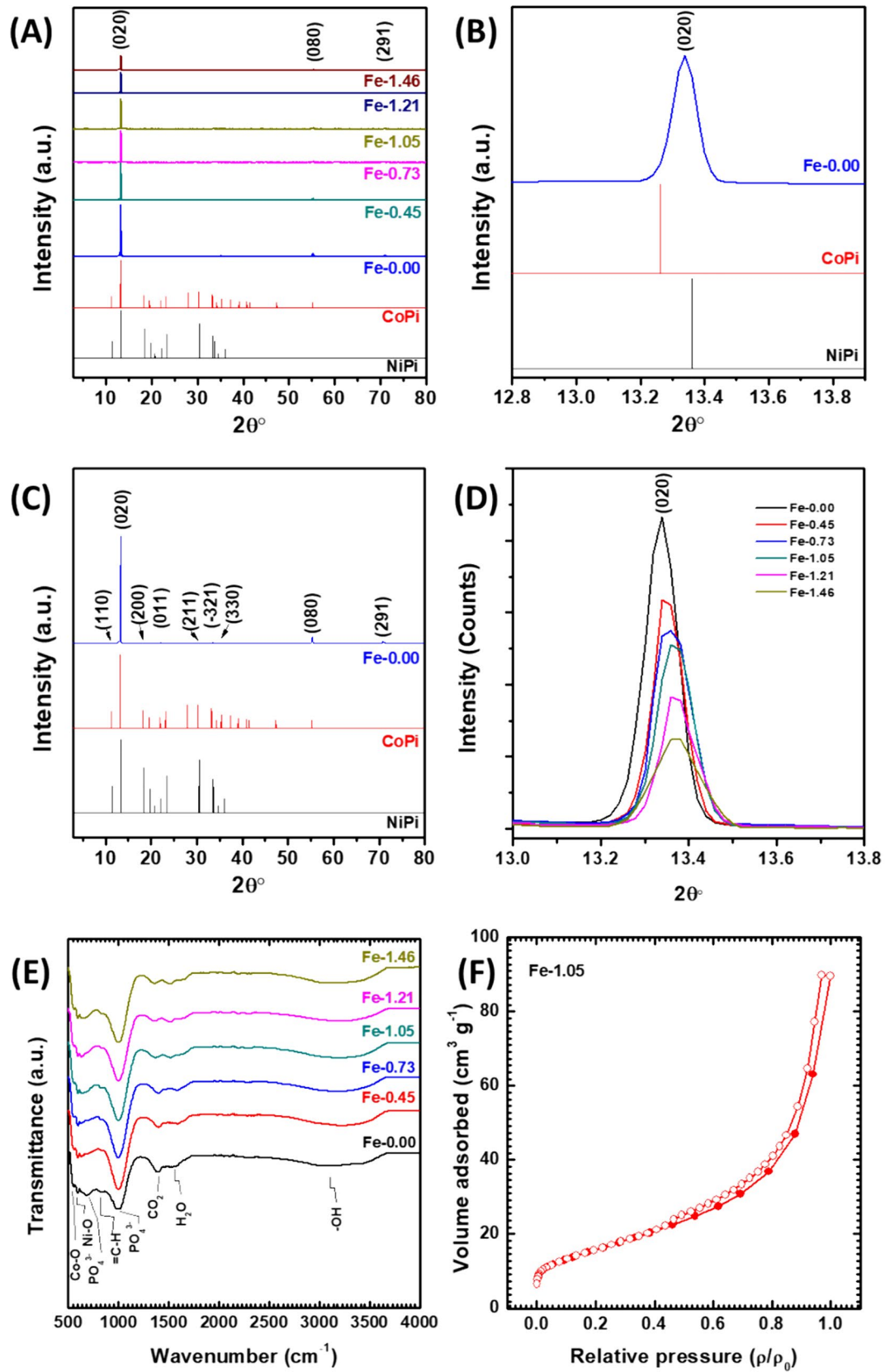
◄**Fig. 2 a** Full scan XRD analysis of Fe-doped nickel cobalt phosphate (Fe-0.00 to Fe-1.46). **b** Enlarged XRD pattern of Fe-0.00. **(c)** Indexing of peaks with Ni/Co phosphate. **(d)** Enlarged XRD pattern to observe peak shift due to Fe doping. **e** FTIR and **f** N_2 adsorption–desorption isotherms of Fe-doped nickel cobalt phosphate

Spectrometer (XPS; K-Alpha, Thermo Scientific, USA), used microfocus monochromatic radiations of Al K_α X-ray.

Electrochemical Experiment

Electrochemical characterization of the samples was performed using an Autolab electrochemical workstation (Metrohm, Netherlands) in a typical three-electrode electrochemical cell configuration. The working electrode was composed of NF (an area of 1 cm^2) with directly deposited iron-doped nickel cobalt phosphate nanofiber. A Hg/HgO electrode (1-M KOH electrolyte inside) and a platinum plate were used as the reference and counter electrodes, respectively. For the OER and HER investigations, a 1-M KOH electrolyte solution with a pH of approximately 13.7 was employed. The recorded voltages were converted from the Hg/HgO electrode ($V_{Hg/HgO}$) reference to the reversible hydrogen electrode (RHE) reference using the $V_{RHE} = V_{SCE} + 0.059pH + V_{Hg/HgO}$ equation. Polarization curves were generated by linear sweep voltammetry (LSV) at a scan rate of 1 mV s^{-1} and reported without iR corrections. For the OER, the potential window ranged from 1.00 to 1.8 V vs. RHE, whereas, for the HER, it extended from 0.00 to −0.50 V vs. RHE. Electrochemical impedance spectroscopy (EIS) was performed with an amplitude of 10 mV across a frequency range of 50 kHz–100 mHz. Long-term catalytic stability assessments were performed through a chronoamperometry (CA) test at specific overpotentials. Overpotentials (η) for the OER were calculated by subtracting the thermodynamic potential value for OER (1.23 V) from the observed potential in terms of RHE. Cyclic voltammetry (CV) curves were recorded to measure the electrochemical surface area (ECSA) within the potential range of 1.035–1.135 V vs. RHE at different scan rates. In a two-electrode system, a full-cell electrolyzer was assembled, with the same material (Fe-1.05) electrodes serving as both the anode and cathode for the characterization of overall water splitting and durability tests in the same alkaline electrolyte.

Results and Discussion

Iron-doped nickel cobalt phosphate nanofibers were hydrothermally synthesized at 130 °C via a bottom-up approach through the controlled assembly of Ni, Co, the dopant Fe cation, and the phosphate anion (PO_4^{3-}) (Fig. 1). The process is highlighted through the use of urea ($CO(NH_2)_2$), which hydrolyzes at high temperatures to slowly release CO_2 and ammonia (NH_3). The formed NH_3 (or NH_4OH) slowly increases pH, allowing the controlled deprotonation of $H_2PO_4^-$ to PO_4^{3-}. Moreover, NH_3 (or NH_4OH) may form a complex ($M(NH_3)_x(H_2O)_{(6-x)}^{2+}$) with metal cations (assuming the formation of an octahedral complex), which then reacts with PO_4^{3-} to form a Fe-doped nickel cobalt phosphate nanofibers.

After the reaction, iron-doped nickel cobalt phosphate was collected and characterized to understand its physico-chemical properties. The PXRD patterns of the as-prepared Fe-0.00, Fe-0.45, Fe-0.73, Fe-1.05, Fe-1.21, and Fe-1.46 samples were collected (Fig. 2a). In Fig. 2b, c, the peak (0 2 0) of the Fe-0.00 sample ($2\theta = 13.34°$, $d = 6.6319$ Å) is observed between NiPi (nickel phosphate hydrate $Ni_3(PO_4)_2·8H_2O$, $2\theta = 13.25°$, JCPDS-33–0951) and CoPi (cobalt phosphate hydrate $Co_3(PO_4)_2·8H_2O$, $2\theta = 13.38°$, JCPDS-33–0432). In addition, the other peaks (1 1 0), (2 0 0), (0 1 1), (2 1 1), (−3 1 2), (3 3 0), (0 8 0), and (2 9 1) are well matched with the JCPDS data, which indicates the formation of nickel cobalt phosphate ($Ni_{3-x}Co_x(PO_4)_2·nH_2O$) in the sample [38]. Upon Fe doping at a minute amount (0.00%–1.46%), the peak (0 2 0) shifted toward a higher angle with an observable decrease in peak intensity (Fig. 2d). In addition, increasing the Fe concentration in the catalyst resulted in a gradual broadening of the (0 2 0) peak.

Next, the FTIR spectra of the iron-doped nickel cobalt phosphate samples (Fe-0.00, Fe-0.45, Fe-0.73, Fe-1.05, Fe-1.21, and Fe-1.46) were collected (Fig. 2e). The peaks at 558 and 596 cm^{-1} are assigned to the stretching vibrations of metal‐oxygen bonding (Co‐O and Ni‐O, respectively) [40, 41]. The peak at 680 cm^{-1} corresponds to the intramolecular asymmetric bending vibrations of the PO_4^{3-} bond [42]. In addition, a small peak at 828 cm^{-1} indicates =C–H bonding, probably arising from urea [43]. Notably, a sharp absorption peak at 1021 cm^{-1} signifies the asymmetric stretching vibrations of PO_4^{3-} [44]. The absorption band at 1394 cm^{-1} suggests the adsorption of CO_2 molecules on the surface [45]. Furthermore, the absorption at 1645 cm^{-1}, along with the broader band at 3450 cm^{-1}, indicates structural water molecules [35].

The N_2 adsorption–desorption isotherms at 77 K of the iron-doped nickel cobalt phosphate nanofibers (Fe-0.00–Fe-1.46) were measured to evaluate BET SAs and pore size distributions (Fig. S1). Accordingly, the adsorption data exhibit type-IV isotherms with a BET SA ranging from ~46 to 57 m^2 g^{-1} [46]. In particular, Fe-1.05 has a maximized BET SA (57.0 m^2 g^{-1}), which is significantly higher than that of samples without Fe (sample Fe-0.00 with a BET SA of 46.2 m^2 g^{-1}) (Figs. 2f and S1). The mesopore distribution of the corresponding samples was then analyzed using the BJH method, yielding a mesopore size of ~3.7 nm (Fig. S2).
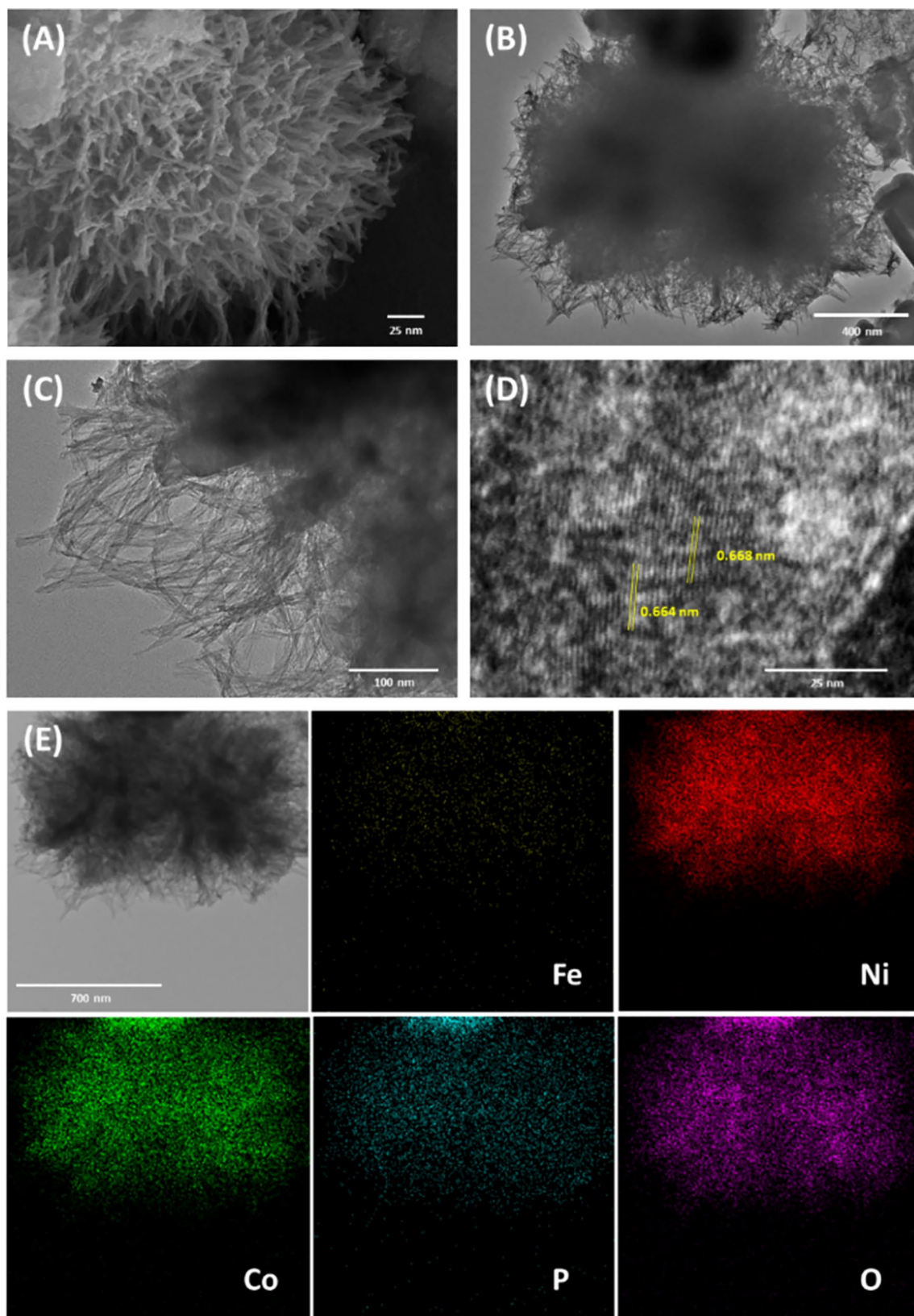
Fig. 3 Morphological analysis. **a** FE-SEM image; **b**, **c** TEM images; **d** HR-TEM image; **e** Elemental mappings of Fe-1.05 sample
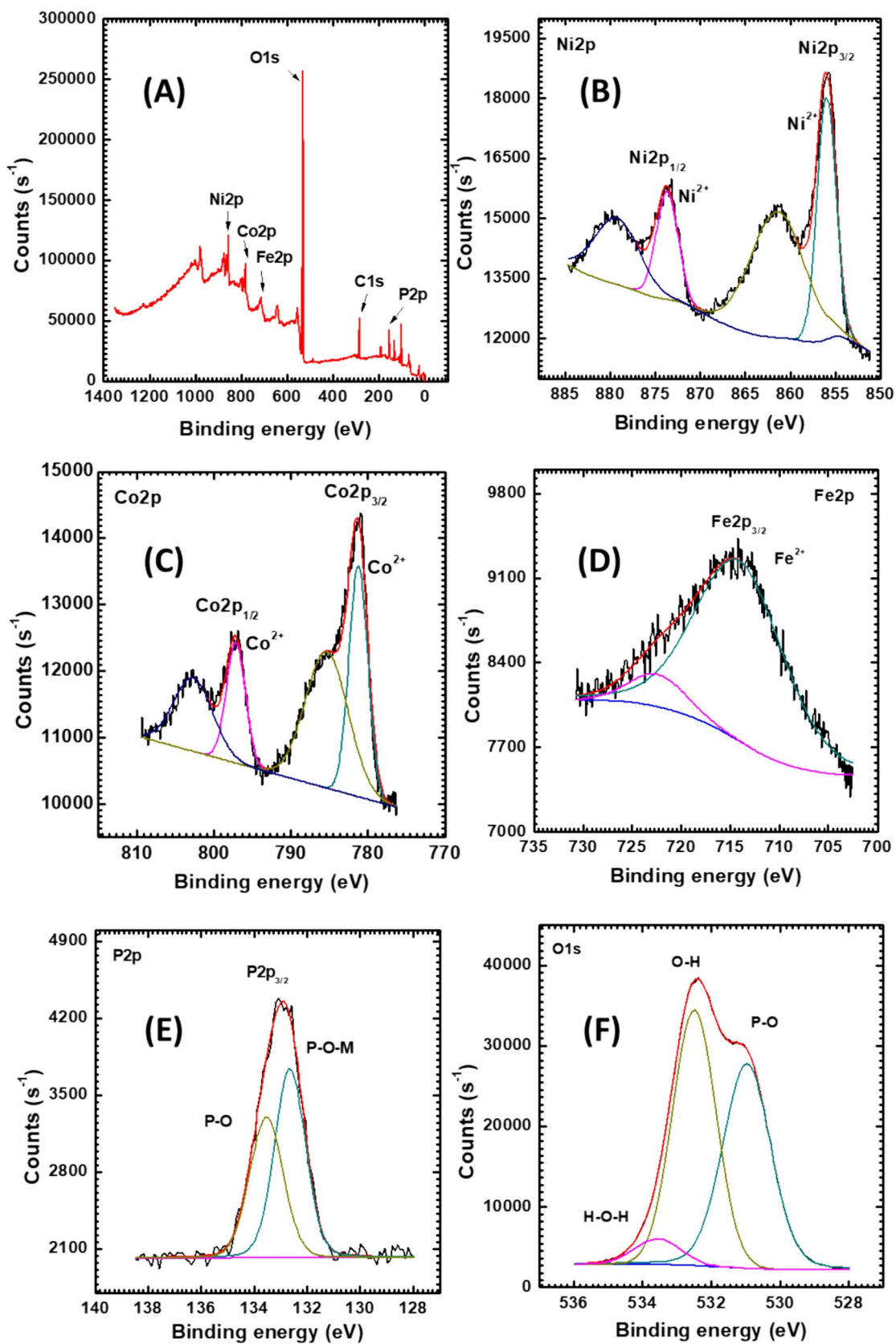
Fig. 4 XPS analysis of Fe-1.05 sample: **a** survey spectrum; high-resolution spectra of **b** Ni2*p*, **c** Co2*p*, **d** Fe2*p*, **e** P2*p*, and **f** O1s
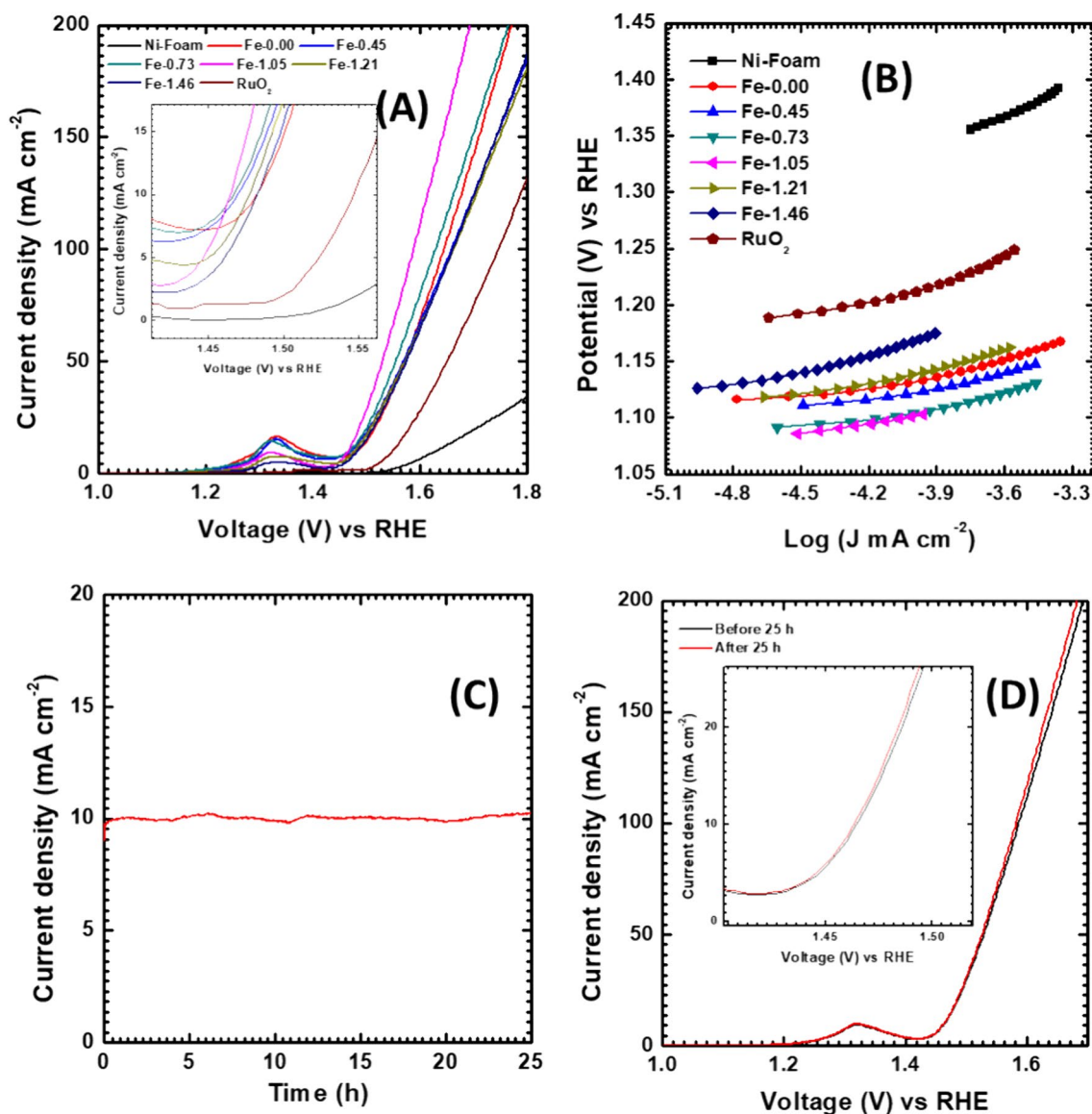
Fig. 5 Electrochemical OER study. **a** LSV plots (inset shows the enlarged LSV plots at knee point); **b** Tafel slopes of iron-doped nickel cobalt phosphate (Fe-0.00–Fe-1.46); **c** 25-h stability test result of the Fe-1.05 electrode; **d** comparison of LSV plots before and after stability test (inset shows the enlarged LSV plots at knee point)

The narrowing peak in the mesopore distribution implied a uniform particle size distribution. The combination of the high BET SA and mesoporous structure of Fe-doped nickel cobalt phosphate nanofibers may improve electrochemical activity by providing numerous active sites and facilitating rapid ion transfer through the mesopores.

We further employed FE-SEM and TEM to analyze the morphology of the iron-doped nickel cobalt phosphate (Fig. 3a−c). The resulting images reveal the nanofiber morphology of the as-prepared iron-doped nickel cobalt phosphate with a cluster size of 1–2 μm, with ∼ 20 nm observed for each hairy nanofiber. The bright- and dark-field TEM images reveal the random orientation and uniform growth of

the nanofibers (Figures S4a and b). In addition, we observed no morphological changes upon iron doping. Energy-dispersive X-ray spectroscopy elemental mapping (from FE-SEM) of all samples was further collected (Fig. S5). The results show a good distribution of Fe, Co, Ni, P, and O throughout the material (Figs. 3e and S5), with the Fe atom% ranging from 0% to 1.46%. In particular, the observed Fe atom% values in Fe-0.00 and Fe-1.05 are 0% and 1.05%, respectively. We further employed HR-TEM to confirm the phase composition of the Fe-doped nickel cobalt phosphate nanofibers (Fig. 3d). The results show discernible fringe patterns with a d-spacing of ∼ 0.66 nm, coinciding with that of the (0 2 0) lattice planes in the PXRD pattern of $Ni_xCo_{3-x}(PO_4)_2 \cdot nH_2O$.
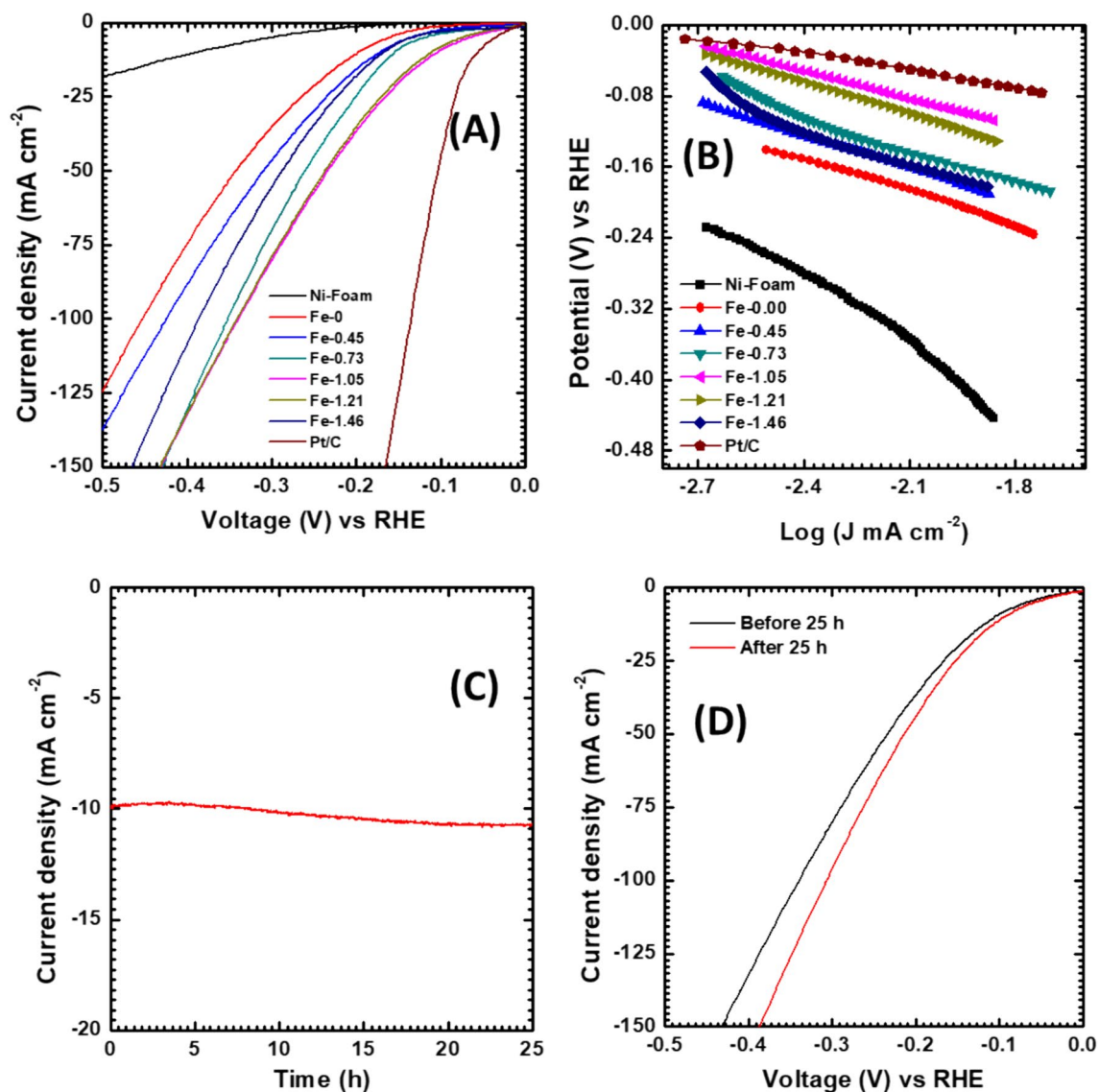
Fig. 6 Electrochemical HER study. **a** LSV plots, **b** Tafel slopes of iron-doped nickel cobalt phosphate (Fe-0.00–Fe-1.46), **c** 25-h stability test result of Fe-1.05 electrode, **d** comparison of LSV plots before and after stability test

The oxidation states of the elements at the surface of the Fe-doped nickel cobalt phosphate nanofiber (sample Fe-1.05) were studied by XPS analysis. The presence of Fe, Co, Ni, C, P, and O in the Fe-1.05 sample was identified from the survey spectra (Fig. 4a). In the high-resolution spectra for nickel, two major peaks are observed at 856.63 and 874.17 eV, along with two satellite peaks at 862.10 and 879.99 eV. These peaks correspond to Ni2$p_{3/2}$ and Ni2$p_{1/2}$ (Fig. 4b), which confirms the Ni^{2+} electronic state [47, 48]. Similarly, in the high-resolution spectra for cobalt, two major peaks are observed at 781.65 and 797.64 eV, along with two satellite peaks at 785.46 and 802.85 eV. These peaks correspond to Co2$p_{3/2}$ and Co2$p_{1/2}$, which confirms the Co^{2+} oxidation state of Co (Fig. 4c) [49]. Furthermore,

the low-intensity Fe2p peak at 713.46 eV is consistent with Fe2$p_{3/2}$, which confirms the Fe^{2+} oxidation state of iron in the Fe-1.05 sample (Fig. 4d). In addition, in the high-resolution XPS spectra for phosphorous, two peaks are observed at 132.66 and 133.53 eV, corresponding to P2$p_{3/2}$ (metal phosphate, P–O–M) and P2$p_{1/2}$ (P–O covalence bond), respectively (Fig. 4e) [50]. As shown in Fig. 4f, the oxygen peak is deconvoluted into three peaks at 530.97, 532.48, and 533.55 eV, corresponding to the P–O, M–O, and H–O–H bonds, respectively, in phosphate and surface-adsorbed water molecules [51–53]. The XPS analyses indicate Ni^{2+}, Co^{2+}, and Fe^{2+} in the Fe-1.05 catalyst.

In the next step, the Fe-doped nickel cobalt phosphate nanofibers were deposited on NF for electrochemical

Table 1 Comparison of this study with previously reported nickel cobalt phosphate and related materials

Material	Electrolyte	Overpotential		Tafel slope (mV dec^{-1})	Stability (h)	Ref
		η (mV)	@ j (mA cm^{-2})			
Ni/Co phosphates	0.5-M H$_2$SO$_4$	160 (HER)	10	57	120	[27]
CuCoNiP	2.0-M NaOH	265 (OER)	10	105.5	1.94	[54]
		340 (OER)	50			
CuCoNiP	2.0-M NaOH	170 (HER)	10	99.6	2.77	[54]
		295 (HER)	100			
CoNi$_2$(PO$_4$)$_2$	1.0-M KOH	347 (OER)	10	35	2	[21]
Ni−Co phosphate	1.0-M KOH	310 (OER)	10	68	16	[22]
Ni–Co hydrogen phosphate	1.0-M KOH	320 (OER)	10	84	15	[23]
(Co$_{0.5}$Ni$_{0.5}$)$_3$(PO$_4$)$_2$	1.0-M KOH	273 (OER)	10	59.3	30	[24]
Fe$_{0.86}$Ni$_{0.14}$-PO$_x$	1.0-M KOH	247 (OER)	10	48.3	100	[55]
		125 (HER)	10	66.2		
Fe-doped Ni$_2$P	1.0-M KOH	260 (OER)	10	35.7	17	[56]
Ni−Co phosphate	3.0-M KOH	378 (OER)	10	60.79	12	[25]
Ni−Co phosphate	1.0-M KOH	309 (OER)	10	54.2	10	[26]
		236 (HER)	10	–		
CoNiPO$_x$@V-Co$_4$N	1.0-M KOH	270 (OER)	10	54.76	50	[28]
		335 (OER)	100			
CoNiPO$_x$@V-Co$_4$N	1.0-M KOH	58 (HER)	10	85.7	50	[28]
Ni−Co phosphate	1.0-M KOH	388 (OER)	10	90.3	15	[57]
Na$_2$Ni$_{0.75}$Fe$_{0.25}$P$_2$O$_7$	1.0-M KOH	300 (OER)	10	110	100	[58]
Ni$_2$P$_4$O$_{12}$	1.0-M KOH	270 (OER)	10	102	100	[59]
NiCoFe phosphate	1.0-M KOH	240 (OER)	10	65	24	[37]
		231 (HER)	10	86		
Fe-doped NiCo phosphate	1.0-M KOH	234 (OER)	10	30.82	25	This study
		298 (OER)	50			
		375 (OER)	100			
Fe-doped NiCo phosphate	1.0-M KOH	104 (HER)	10	103.31	25	This study
		233 (HER)	50			
		339 (HER)	100			

overall water splitting using a procedure similar to that used for the synthesis of the powder samples. The OER performance of the Fe-doped nickel cobalt phosphate nanofibers deposited on NF was then investigated. LSV analyses were performed to evaluate the catalytic activity in a 1-M KOH electrolyte at a scan rate of 1 mV s^{-1} (Fig. 5a). The overpotentials recorded for the Fe-0.00, Fe-0.45, Fe-0.73, Fe-1.05, Fe-1.21, and Fe-1.46 catalyst electrodes to deliver a current density of 10 mA cm^{-2} were 252, 240, 237, 234, 247, and 253 mV, respectively. In comparison, the commercially available RuO$_2$ and NF exhibit respective overpotentials of 316 and 399 mV (@ 10 mA cm^{-2}), which are higher than that of Fe-1.05@NF (234 mV). The Fe cation in the nickel-cobalt phosphate nanofiber enhances the electrochemical activity. Interestingly, the optimized sample (Fe-1.05@NF) requires overpotentials of 234, 298, and 375 mV to deliver current

densities of 10, 50, and 100 mA cm^{-2}, respectively. These values demonstrate the superior OER performance of Fe-1.05@NF over previously reported nickel cobalt phosphate catalysts [21–28].

The Tafel slopes for NF, Fe-0.00, Fe-1.05, and RuO$_2$ were then computed as 91.03, 38.60, 30.82, and 55.37 mV dec^{-1}, respectively (Fig. 5b). The small Tafel slope value of the Fe-1.05@NF electrode suggests faster and highly efficient kinetics of OER at its surface. EIS was performed to explore the electrochemical kinetics activity. The Nyquist plots of the Fe-0.00 and Fe-1.05@NF samples were fitted with an equivalent circuit (Fig. S6). The charge transfer resistance (R_{ct}) values are 9.05 and 3.91 Ω for Fe-0.00 and Fe-1.05@NF, respectively. All resistance values are listed in Table S1. The low R_{ct} value of Fe-1.05@NF indicates fast charge transfer and reaction
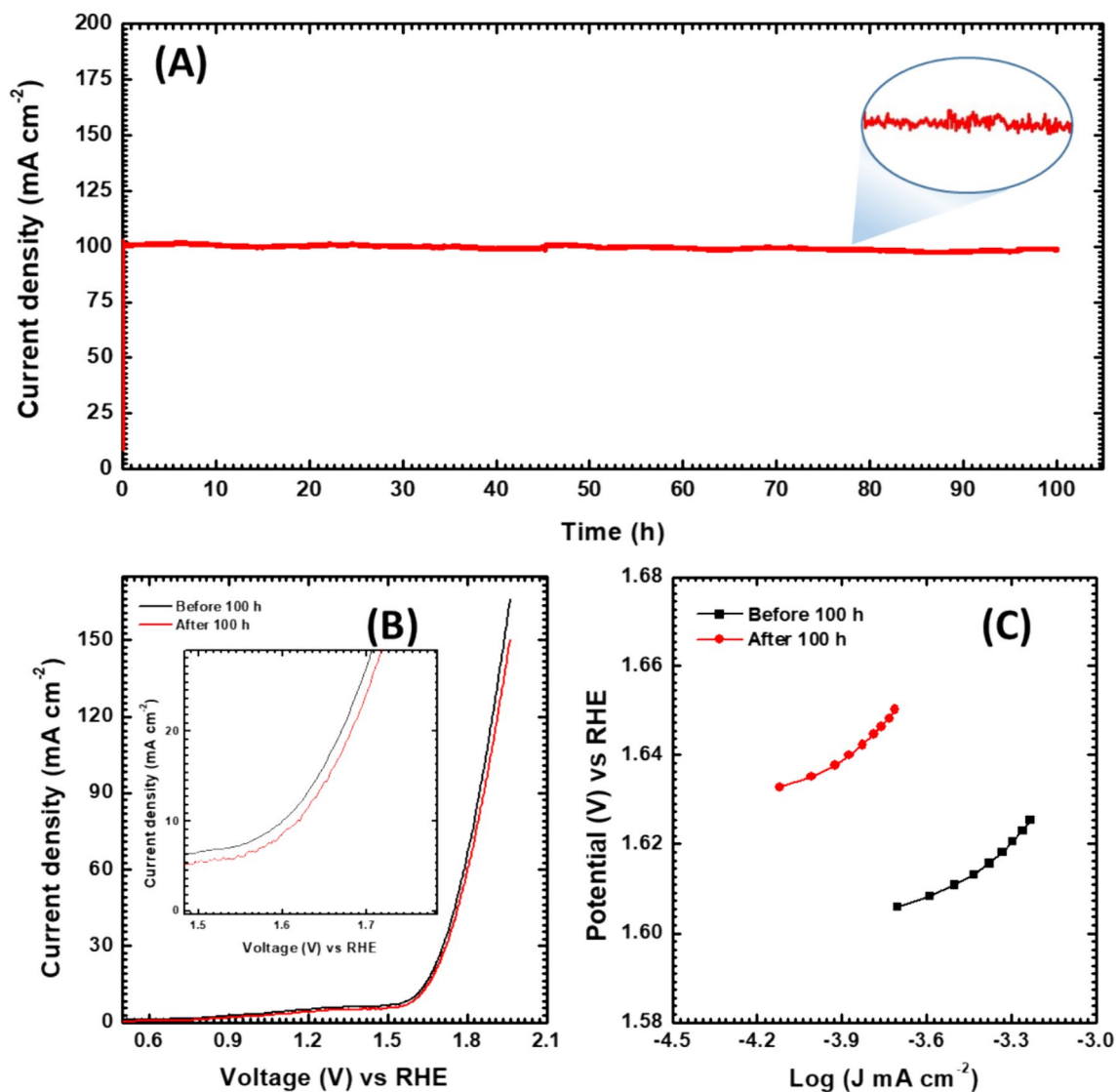
Fig. 7 **a** Electrochemical overall water splitting stability study of Fe-1.05 electrode in 1-M KOH electrolyte; **b** comparative LSV plots; **c** comparative Tafel slopes before and after 100 h of catalysis

Table 2 Comparative study of existing full-cell water splitting electrolysis devices and this study

Material	Electrolyte	Potential		Tafel slope (mV dec^{-1})	Stability (h)	Reference
		(V)	@ j (mA cm^{-2})			
$Fe_{0.86}Ni_{0.14}$-PO_x	1.0-M KOH	1.66	10	–	100	[55]
Ni−Co phosphate	1.0-M KOH	1.745	10	–	–	[26]
$CoNiPO_x$@V-Co_4N	1.0-M KOH	1.52	10	–	50	[28]
Co:FePi	1.0-M KOH	2.04	10	–	96	[35]
CoFe phosphate	1.0-M KOH	1.75	10	32.5	100	[61]
Fe-doped NiCo phosphate	1.0-M KOH	1.59	10	41.18	100	**This study**
		1.76	50			
		1.86	100			

kinetics, confirming the positive effect of the Fe dopant in the nickel-cobalt phosphate nanofiber.

The OER stability of Fe-1.05@NF in a 1-M KOH electrolyte was then investigated using a three-electrode setup at an overpotential to achieve a current density of 10 mA cm^{-2} for 25 h (Fig. 5c). The results show a negligible change in the current density during the investigation period. The LSV plots before and after 25 h of catalysis reveal a negligible change (Fig. 5d). This result proves the high stability of Fe-1.05@NF for OER. The comparative Tafel slopes before and after 25 h of catalysis are shown in Fig. S7, indicating a similar reaction rate during the investigation period. Moreover, the Nyquist plots from the EIS measurements reveal almost no change in R_{ct} (Fig. S8). These results fully confirm the stability of Fe-1.05@NF for OER.

Furthermore, we analyzed the HER performance of Fe-1.05@NF. The LSV curves are shown in Fig. 6a. The overpotentials (@ 10 mA cm^{-2}) of bare NF, Fe-0.00@NF, Fe-1.05@NF, and Pt/C are 388, 198, 104, and 57.2 mV, respectively. The Pt/C electrode exhibits excellent HER performance, whereas the bare NF exhibits poor HER performance. Moreover, Fe-1.05@NF exhibits overpotentials of 104, 233, and 339 mV to achieve current densities of 10, 50, and 100 mA cm^{-2}, respectively. In addition, the Tafel slopes of NF, Fe-0.00, Fe-1.05@NF, and Pt/C are 266.4, 124.93, 103.31, and 62.66 mV dec^{-1}, respectively (Fig. 6b). The smaller Taffel slope of Fe-1.05 than that of Fe-0.00 indicates a faster HER rate, highlighting the benefit of the Fe cation in the catalyst.

The HER stability of Fe-1.05@NF was then investigated at an overpotential to achieve a current density of −10 mA cm^{-2} for 25 h (Fig. 6C). The results show a negligible change in the current density during the investigation period. Moreover, the LSV analysis of Fe-1.05@NF after the stability test showed only a small change compared with the original sample (Fig. 6d). The overpotential (@10 mA cm^{-2}) of Fe-1.05@NF after the stability test was 93 mV, which is a slight decrease compared with that of the fresh sample (104 mV). Moreover, the slight increase in the reaction rate of Fe-1.05@NF after stability (Tafel slope of 102.47 mV dec^{-1}) after 25 h of catalysis can be attributed to the activation of catalytic sites (Fig. S9).

The overall OER and HER performance of the Fe-1.05@NF electrode before and after 25 h of catalysis is shown in Table S2, which confirmed the excellent performance and structural stability of Fe-1.05@NF. The as-prepared Fe-doped nickel cobalt phosphate electrode (Fe-1.05@NF) exhibits outstanding electrochemical OER and HER performance compared with nickel cobalt phosphate materials reported in the literature (Table 1). In particular, our nanofiber-based catalyst (Fe-1.05@NF) exhibits superior performance over the 2D nanosheet-based NiCoFe phosphate (OER and HER overpotentials of 240 and 231 mV, respectively) (Table 1) [37]. The enhanced electrochemical activity of Fe-1.05@NF can be attributed to the synergistic effect between the metal atoms and phosphate ligands, which facilitates favorable conditions for the adsorption and oxidation of electrolyte ions, enhanced electrical conductivity, active sites availability due to Fe (dopant) metal atoms, alongside a nanostructured (nanofiber) morphology with high porosity.

We further investigated the electrochemically active surface area (EASA) of Fe-1.05@NF. CV curves were then recorded in a small potential window (non-Faradic region) at different scan rates (Fig. S10a−f). C_{dl} is calculated by plotting the anodic charging currents (i_c) of each CV curve against the scan rate (v), as shown in Fig. S11, using Eq. (1).

$$i_c = vC_{dl} \tag{1}$$

The calculated C_{dl} values for the Fe-0.00 and Fe-1.05@NF electrodes are 3.69 and 14.34 mF, respectively. The EASA can be calculated by dividing the C_{dl} values by the specific capacitance (C_s) of the atomically smooth planar real surface area (1 cm^2) of the material under identical electrolyte conditions, where $C_s = 0.04$ mF in alkaline solutions [60]. The EASA values of the Fe-0.00 and Fe-1.05@NF electrodes are 92.25 and 358.50 cm^2, respectively (Fig. S12). The roughness factor (RF) was then calculated by dividing the ECSA by the geometric area of the electrode (the area of the used film is 1 cm^2). The RF values of the Fe-0.00 and Fe-1.05@NF electrodes are 92.25 and 358.50, respectively. The high ECSA and RF values of Fe-1.05 support the high electrochemical performance of Fe-1.05@NF and are consistent with the BET SA analysis.

A long-term water-splitting stability test was conducted for Fe-1.05@NF to investigate its robustness. We investigated full-cell water splitting by employing Fe-1.05@NF as the catalyst material for both the cathode and anode. In this study, LSV (@ 1 mV s^{-1} scan rate) was performed in a potential window of 0–2 V for overall water splitting. Long-term electrolysis was investigated at this potential to attain a current density of 50 mA cm^{-2} for 50 h. The CA I-t curves show the stability of Fe-1.05@NF (Fig. S13). We further investigated high-rate full-cell water splitting at a current density of 100 mA cm^{-2} and pH of 13.7 for 100 h to demonstrate the practical use of Fe-1.05@NF (Fig. 7A). The resulting CA I-t curve reveals the high stability of Fe-1.05@NF under the investigation conditions. LSV was measured before and after 100 h of catalysis (Fig. 7B). The potentials of Fe-1.05@NF after the stability test were 1.61, 1.77, and 1.88 V at 10, 50, and 100 mA cm^{-2}, respectively. These values are slight increases compared with those of the fresh sample (1.59, 1.76, and 1.86 V, respectively). PXRD analysis of Fe-1.05@NF after the stability test for 100 h confirmed the preservation of its structural integrity (Fig. S14).

FE-SEM revealed the unchanged morphology of Fe-1.05@ NF after 100 h of catalysis (Fig. S15). We further compared the Tafel slope and R_{ct} of Fe-1.05@NF before and after 100 h of catalysis (Fig. 7c and S16), showing only a slight increase in the Tafel slope (from 41.18 to 42.70 mV dec^{-1}) and R_{ct} (from 0.079 to 0.082 Ω). The XPS analysis of Fe-1.05@NF after 100 h of catalysis showed only a partial change in oxidation from 2 + to 3 + states (Fig. S17). These results highlight the high performance and durability of Fe-1.05@NF compared with those of the best phosphate-based catalysts in the literature for water splitting (Table 2).

Conclusions

In summary, Fe-doped nickel cobalt phosphate nanofibers were synthesized and deposited on NF. The Fe-1.05@NF sample with an Fe atom% of 1.05 exhibited the highest electrochemical OER activity (η = 234 mV @ 10 mA cm^{-2}) and HER activity (η = 104 mV @ 10 mA cm^{-2}). This high-performance Fe-1.05 electrode was used for overall water splitting in an alkaline electrolyte (pH = 13.7) and delivered a current density of 10 mA cm^{-2} at an overpotential of 1.59 V. The long-duration (100 h) overall water-splitting study revealed the robustness and high stability of the synthesized catalyst material in an alkaline medium. This study proves that Fe-doped nickel cobalt phosphate nanofibers are promising candidates for overall water splitting because of their robust and superior catalysis performance over other catalysts for water splitting.

References

1. S. Schlussel, S. Kwon, A review of formic acid decomposition routes on transition metals for its potential use as a liquid H$_2$ carrier. Korean J. Chem. Eng. **39**, 2883 (2022)
2. Y. Cheng, W. Zhang, B. Shi, S. Li, B. Dong, Y. Quan, X. Ji, Improved the hydrogen sorption properties of MgH$_2$ by CeMnZr solid solution. Korean J. Chem. Eng. **40**, 104 (2023)
3. X. Zou, Y. Zhang, Noble metal-free hydrogen evolution catalysts for water splitting. Chem. Soc. Rev. **44**, 5148 (2015)
4. X.F. Lu, L.F. Gu, J.W. Wang, J.X. Wu, P.Q. Liao, G.R. Li, Bimetal-organic framework derived CoFe$_2$O$_4$/C porous hybrid nanorod arrays as high-performance electrocatalysts for oxygen evolution reaction. Adv. Mater. **29**, 1604437 (2017)
5. L. Cao, Q. Luo, J. Chen, L. Wang, Y. Lin, H. Wang, X. Liu, X. Shen, W. Zhang, W. Liu et al., Dynamic oxygen adsorption on single-atomic Ruthenium catalyst with high performance for acidic oxygen evolution reaction. Nat. Commun. **10**, 4849 (2019)
6. S. Siracusano, N.V. Dijk, E.P. Johnson, V. Baglio, A.S. Aricò, Nanosized IrO$_x$ and IrRuO$_x$ electrocatalysts for the O$_2$ evolution reaction in PEM water electrolysers. Appl. Catal. B Environ. **164**, 488 (2015)
7. S. Cherevko, S. Geiger, O. Kasian, N. Kulyk, J.P. Grote, A. Savan, B.R. Shrestha, S. Merzlikin, B. Breitbach, A. Ludwig et al., Oxygen and hydrogen evolution reactions on Ru, RuO$_2$, Ir, and IrO$_2$ thin film electrodes in acidic and alkaline electrolytes: a comparative study on activity and stability. Catal. Today **262**, 170 (2016)
8. L. Li, P. Wang, Q. Shao, X. Huang, Metallic nanostructures with low dimensionality for electrochemical water splitting. Chem. Soc. Rev. **49**, 3072 (2020)
9. F.F. Alharbi, Z. Ahmad, A.H. Chughtai, R.Y. Khosa, H.M. Tahir Farid, Designing CuSe-gCN nanocomposite as an active electrocatalyst for water oxidation. Korean J. Chem. Eng. **40**, 2303 (2023)
10. T.N. Tu, S.A. Khalate, K. Chang, J. Kim, "Ship-in-a-bottle" entrapment of biomolecules in MOF-based xerogel monoliths for high-performance electrochemical hydrogen evolution. J. Mater. Chem. A **12**, 7622 (2024)
11. Q.H. Nguyen, V.D.C. Tinh, S. Oh, T.M. Pham, T.N. Tu, D. Kim, J. Han, K. Im, J. Kim, Metal-organic framework-polymer complex-derived single-atomic oxygen reduction catalyst for anion exchange membrane fuel cells. Chem. Eng. J. **48**, 148508 (2024)
12. A.H. Al-Naggar, N.M. Shinde, J.S. Kim, R.S. Mane, Water splitting performance of metal and non-metal-doped transition metal oxide electrocatalysts. Coord. Chem. Rev. **474**, 214864 (2023)
13. S. Nagappan, S. Yang, A. Adhikari, R. Patel, S. Kundu, A review on consequences of flexible layered double hydroxide-based electrodes: Fabrication and water splitting application. Sustain. Energy Fuels **7**, 3741 (2023)
14. H. Su, J. Jiang, S. Song, B. An, N. Li, Y. Gao, L. Ge, Recent progress on design and applications of transition metal chalcogenide-associated electrocatalysts for the overall water splitting. Chin. J. Catal. **44**, 7 (2023)
15. M. Batool, A. Hameed, M.A. Nadeem, Recent developments on iron and nickel-based transition metal nitrides for overall water splitting: A critical review. Coord. Chem. Rev. **480**, 215029 (2023)
16. H. Yin, F. Rong, Y. Xie, A review of typical transition metal phosphides electrocatalysts for hydrogen evolution reaction. Int. J. Hydrogen Energy **52**, 350 (2023)
17. Q.H. Nguyen, K. Im, T.N. Tu, J. Park, J. Kim, ZIF67-derived ultrafine Co$_9$S$_8$ nanoparticles embedded in nitrogen-doped hollow carbon nanocages for enhanced performances of trifunctional ORR/OER/HER and overall water splitting. Carbon Lett. (2024). https://doi.org/10.1007/s42823-024-00733-1
18. L. Yana, H. Wanga, J. Shen, J. Ning, Y. Zhong, Y. Hu, Formation of mesoporous Co/CoS/Metal-N-C@S, N-codoped hairy carbon polyhedrons as an efficient trifunctional electrocatalyst for Zn-air batteries and water splitting. Chem. Eng. J. **403**, 126385 (2021)
19. Y. Zhang, J. Wu, B. Guo, H. Huo, S. Niu, S. Li, P. Xu, Recent advances of transition-metal metaphosphates for efficient electrocatalytic water splitting. Carbon Energy **5**, e375 (2023)
20. S.A. Khalate, S.A. Kadam, Y.R. Ma, S.S. Pujari, S.J. Marje, P.K. Katkar, A.C. Lokhande, U.M. Patil, Hydrothermally synthesized iron phosphate hydroxide thin film electrocatalyst for electrochemical water splitting. Electrochim. Acta **319**, 118 (2019)

21. J. Zhang, Y. Yang, Z. Zhang, X. Xua, X. Wang, Rapid synthesis of mesoporous $Ni_xCo_3-x(PO_4)_2$ hollow shells showing enhanced electrocatalytic and supercapacitor performance. J. Mater. Chem. A **2**, 20182 (2014)

22. N.L.W. Septiani, Y.V. Kaneti, K.B. Fathoni, K. Kani, A.E. Allah, B. Yuliarto, Nugraha, H.K. Dipojono, Z.A. Alothman, D. Golberg et al., Self-assembly of two-dimensional bimetallic nickel–cobalt phosphate nanoplates into one-dimensional porous chainlike architecture for efficient oxygen evolution reaction. Chem. Mater. **32**, 7005 (2020)

23. N.L.W. Septiani, Y.V. Kaneti, K.B. Fathoni, Y. Guo, Y. Ide, B. Yuliarto, X. Jiang, Nugraha, H.K. Dipojono, D. Golberg et al., Tailorable nanoarchitecturing of bimetallic nickel–cobalt hydrogen phosphate via the self-weaving of nanotubes for efficient oxygen evolution. J. Mater. Chem. A **8**, 3035 (2020)

24. J. Li, W. Xu, D. Zhou, J. Luo, D. Zhang, P. Xu, L. Wei, D. Yuan, Synthesis of 3D flower-like cobalt nickel phosphate grown on Ni foam as an excellent electrocatalyst for the oxygen evolution reaction. J. Mater. Sci. **53**, 2077 (2018)

25. D. Wang, Y. Wang, Z. Fu, Y. Xu, L.X. Yang, F. Wang, X. Guo, W. Sun, Z.L. Yang, Cobalt–nickel phosphate composites for the all-phosphate asymmetric supercapacitor and oxygen evolution reaction. ACS Appl. Mater. Interfaces **13**, 34507 (2021)

26. Y. Meng, M. Wang, Z. Zhu, T. Jiang, Z. Liu, N. Chen, C. Shen, Q. Peng, W. Chen, Multifunctional nickel-cobalt phosphates for high-performance hydrogen gas batteries and self-powered water splitting. ACS Appl. Energy Mater. **4**, 12927 (2021)

27. Y. Xu, R. Wang, Y. Zheng, L. Zhang, T. Jiao, Q. Peng, Z. Liu, Facile preparation of self-assembled Ni/Co phosphates composite spheres with highly efficient HER electrocatalytic performances. Appl. Surf. Sci. **509**, 145383 (2020)

28. T.I. Singh, A. Maibam, D.C. Cha, S. Yoo, R. Babarao, S.U. Lee, S. Lee, High-alkaline water-splitting activity of mesoporous 3D heterostructures: an amorphous-shell@crystalline-core nanoassembly of Co-Ni-phosphate ultrathin-nanosheets and V-doped cobalt-nitride nanowires. Adv. Sci. **9**, 2201311 (2022)

29. Z. Zhang, J. Zhang, T. Wang, Z. Li, G. Yang, H. Bian, J. Lia, D. Gao, Durable oxygen evolution reaction of one dimensional spinel $CoFe_2O_4$ nanofibers fabricated by electrospinning. RSC adv. **8**, 5338 (2018)

30. X. Cao, T. Wang, L. Jiao, Transition-metal (Fe Co, and Ni)-based nanofiber electrocatalysts for water splitting. Adv. Fiber Mater. **3**, 210 (2021)

31. C.Z. Yuan, S. Huang, H. Zhao, J. Li, L. Zhang, Y. Weng, T.Y. Cheang, H. Yin, X. Zhang, S. Ye, Vacancy defect tuning of electronic structures of transition metal (hydr) oxide-based electrocatalysts for enhanced oxygen evolution. Energy Adv. **2**, 73–85 (2023)

32. Q. Wang, R. He, F. Yang, X. Tian, H. Sui, L. Feng, An overview of heteroatom doped cobalt phosphide for efficient electrochemical water splitting. Chem. Eng. J. **456**, 141056 (2023)

33. Y. Wang, Y. Jiang, Y. Zhao, X. Ge, Q. Lu, T. Zhang, D. Xie, M. Li, Y. Bu, Design strategies of perovskite nanofibers electrocatalysts for water splitting: a mini review. Chem. Eng. J. **451**, 138710 (2023)

34. L. Trotochaud, S.L. Young, J.K. Ranney, S.W. Boettcher, Nickel–iron oxyhydroxide oxygen-evolution electrocatalysts: the role of intentional and incidental iron incorporation. J. Am. Chem. Soc. **136**, 6744 (2014)

35. S.A. Khalate, S.A. Kadam, Y.R. Ma, S.S. Pujari, U.M. Patil, Cobalt doped iron phosphate thin film: an effective catalyst for electrochemical water splitting. J. Alloys Compd. **885**, 160914 (2021)

36. J. Chen, G. Zhao, Y. Chen, K. Rui, H. Mao, S.X. Dou, W. Sun, Iron-doped nickel molybdate with enhanced oxygen evolution kinetics. Chem. Eur. J. **25**, 280 (2019)

37. M.A.Z.G. Sial, H. Lin, X. Wang, Microporous 2D NiCoFe phosphate nanosheets supported on Ni foam for efficient overall water splitting in alkaline media. Nanoscale **10**, 12975 (2018)

38. S.J. Marje, V.V. Patil, V.G. Parale, H.H. Park, P.A. Shinde, J.L. Gunjakar, C.D. Lokhande, U.M. Patil, Microsheets like nickel cobalt phosphate thin films as cathode for hybrid asymmetric solid-state supercapacitor: Influence of nickel and cobalt ratio variation. Chem. Eng. J. **429**, 132184 (2022)

39. J. He, L. Sun, K. Zhang, W. Wang, J. Jiang, Y. Chen, P. Yang, J. Chu, Effect of post-sulfurization on the composition, structure and optical properties of Cu_2ZnSnS_4 thin films deposited by sputtering from a single quaternary target. Appl. Surf. Sci. **264**, 133 (2013)

40. T.T. Nguyen, V.H. Nguyen, R.K. Deivasigamani, D. Kharismadewi, Y. Iwai, J.J. Shim, Facile synthesis of cobalt oxide/reduced graphene oxide composites for electrochemical capacitor and sensor applications. Solid State Sci. **53**, 71 (2016)

41. S.T. Navale, V.V. Mali, S.A. Pawar, R.S. Mane, M. Naushad, F.J. Stadlerd, V.B. Patil, Electrochemical supercapacitor development based on electrodeposited nickel oxide film. RSC adv. **5**, 51961 (2015)

42. C.M. Burba, R. Frech, Vibrational spectroscopic investigation of structurally-related $LiFePO_4$, $NaFePO_4$, and $FePO_4$ compounds. Spectrochim. Acta A Mol. Biomol. Spectrosc. **65**, 44 (2006)

43. B.M. Lee, V.T. Bui, H.S. Lee, S.K. Hong, H.S. Choi, J.H. Choi, Fabrication of hexagonally arranged porous carbon films by proton beam irradiation and carbonization. Radiat. Phys. Chem. **163**, 18 (2019)

44. C. Murugesan, S. Lochab, B. Senthilkumar, P. Barpanda, Earth-abundant alkali iron phosphates (AFePO4) as efficient electrocatalysts for the oxygen reduction reaction in alkaline solution. ChemCatChem **10**, 1122 (2018)

45. H.B. Li, M.H. Yu, X.H. Lu, P. Liu, Y. Liang, J. Xiao, Y.X. Tong, G.W. Yang, Amorphous cobalt hydroxide with superior pseudocapacitive performance. ACS Appl. Mater. Interfaces **6**, 745 (2014)

46. J.B. Condon, *Surface Area and Porosity Determinations by Physisorption: Measurement, Classical Theories and Quantum Theory* (Elsevier, 2020). https://doi.org/10.1016/C2018-0-00544-7

47. S.J. Marje, S.S. Pujari, S.A. Khalate, V.V. Patil, V.G. Parale, T. Kim, H.H. Park, J.L. Gunjakar, C.D. Lokhandea, U.M. Patil, Intercalation-type pseudocapacitive clustered nanoparticles of nickel–cobalt phosphate thin films synthesized via electrodeposition as cathode for high-performance hybrid supercapacitor devices. J. Mater. Chem. A **10**, 11225 (2022)

48. J. Chang, Q. Lv, G. Li, J. Ge, C. Liu, W. Xing, Core-shell structured $Ni_{12}P_5/Ni_3(PO_4)_2$ hollow spheres as difunctional and efficient electrocatalysts for overall water electrolysis. Appl. Catal. B Environ. **204**, 486 (2017)

49. Y. Li, Z. Wang, J. Hu, S. Li, Y. Du, X. Han, P. Xu, Metal–organic frameworks derived interconnected bimetallic metaphosphate nanoarrays for efficient electrocatalytic oxygen evolution. Adv. Funct. Mater. **30**, 1910498 (2020)

50. R. Gresch, W.M. Warmuth, H. Dutz, X-ray photoelectron spectroscopy of sodium phosphate glasses. J. Non-Cryst. Solids **34**, 127 (1979)

51. T. Sun, L. Xu, Y. Yan, A.A. Zakhidov, R.H. Baughman, J. Chen, Ordered mesoporous nickel sphere arrays for highly efficient electrocatalytic water oxidation. ACS Catal. **6**, 1446 (2016)

52. P. Feng, X. Cheng, J. Li, X. Luo, Calcined nickel-cobalt mixed metal phosphonate with efficient electrocatalytic activity for oxygen evolution reaction. ChemistrySelect **3**, 760 (2018)

53. M.S. Kim, D.T. Tran, T.H. Nguyen, V.A. Dinh, N.H. Kim, J.H. Lee, Ni single atoms and Ni phosphate clusters synergistically triggered surface-functionalized MoS_2 nanosheets for high-performance freshwater and seawater electrolysis. Energy Environ. Mater. **5**, 1340 (2022)

54. B.N. Khiarak, M. Golmohammad, M.M. Shahraki, A. Simchi, Facile synthesis and self-assembling of transition metal phosphide nanosheets to microspheres as a high-performance electrocatalyst for full water splitting. J. Alloys Compd. **875**, 160049 (2021)

55. L. Wang, H. Yu, Z. Huang, Z. Luo, T.T. Isimja, S. Xu, X. Yang, Interface engineering of porous nickel-iron phosphates with enriched oxygen vacancies as an efficient bifunctional electrocatalyst for high current water splitting. Electrochim. Acta **443**, 141932 (2023)

56. J. Li, S. Li, J. Pu, C. Zhong, Q. Zhou, Z. Shen, H. Zhang, H. Ma, Electronic modulation of nickel phosphide by iron doping and its assembly on a graphene framework for efficient electrocatalytic water oxidation. J. Alloys Compd. **824**, 153913 (2020)

57. P. Bhanja, Y. Kim, B. Paul, J. Lin, S.M. Alshehri, T. Ahamad, Y.V. Kaneti, A. Bhaumik, Y. Yamauchi, Facile synthesis of nanoporous transition metal-based phosphates for oxygen evolution reaction. ChemCatChem **12**, 2091 (2020)

58. H.J. Song, H. Yoon, B. Ju, D.W. Kim, Sodium-nickel pyrophosphate as a novel oxygen evolution electrocatalyst in alkaline medium. J. Am. Ceram. Soc. **103**, 4748 (2020)

59. J. Huang, Y. Sun, Y. Zhang, G. Zou, C. Yan, S. Cong, T. Lei, X. Dai, J. Guo, R. Lu et al., A new member of electrocatalysts based on nickel metaphosphate nanocrystals for efficient water oxidation. Adv. Mater. **30**, 1705045 (2018)

60. C.C.L. McCrory, S. Jung, J.C. Peters, T.F. Jaramillo, Benchmarking heterogeneous electrocatalysts for the oxygen evolution reaction. J. Am. Chem. Soc. **135**, 16977 (2013)

61. S.A. Khalate, S.A. Kadam, Y.R. Ma, S.B. Kulkarni, V.G. Parale, U.M. Patil, Binder free cobalt iron phosphate thin films as efficient electrocatalysts for overall water splitting. J. Colloid Interface Sci. **613**, 720 (2022)